

See discussions, stats, and author profiles for this publication at: <https://www.researchgate.net/publication/264256480>

# The Influence of the Solvent Evaporation Rate on the Phase Separation and Electrical Performances of Soluble Acene-Polymer Blend Semiconductors

ARTICLE *in* ADVANCED FUNCTIONAL MATERIALS · JANUARY 2012

Impact Factor: 11.81 · DOI: 10.1002/adfm.201101159

---

CITATIONS

23

---

READS

24

## 8 AUTHORS, INCLUDING:



[Seung Goo Lee](#)

Massachusetts Institute of Technology

22 PUBLICATIONS 535 CITATIONS

[SEE PROFILE](#)

# The Influence of the Solvent Evaporation Rate on the Phase Separation and Electrical Performances of Soluble Acene-Polymer Blend Semiconductors

Wi Hyoung Lee, Donghoon Kwak, John E. Anthony, Hwa Sung Lee, Hyun Ho Choi,  
Do Hwan Kim, Seung Goo Lee, and Kilwon Cho\*

The phase-separation characteristics of spin-cast difluorinated-triethylsilylethynyl anthradithiophene (F-TESADT)/poly(methyl methacrylate) (PMMA) blends are investigated with the aim of fabricating transistors with a high field-effect mobility and stability. It is found that the presence of PMMA in the F-TESADT/PMMA blends prevents dewetting of F-TESADT from the substrate and provides a platform for F-TESADT molecules to segregate and crystallize at the air-film interface. By controlling the solvent evaporation rate of the spin-cast blend solution, it is possible to regulate the phase separation of the two components, which in turn determines the structural development of the F-TESADT crystals on PMMA. At a low solvent evaporation rate, a bilayer structure consisting of highly ordered F-TESADT crystals on the top and low-trap PMMA dielectric on the bottom can be fabricated by a one-step spin-casting process. The use of F-TESADT/PMMA blend films in bottom gate transistors produces much higher field-effect mobilities and greater stability than homo F-TESADT films because the phase-separated interface provides an efficient pathway for charge transport.

## 1. Introduction

Organic thin-film transistors (OTFTs) based on solution-processed organic semiconductors have been investigated over the last decade because of their applications in display backplanes.<sup>[1,2]</sup> Among the solution-processed organic semiconductors, small

molecular semiconductors with solubilizing side groups have attracted much attention because of their high field-effect mobility and solution-processability.<sup>[3–5]</sup> There have been several reviews of the molecular design and characteristics of solution-processed small molecular semiconductors.<sup>[6]</sup> However, the solution processing of these small molecular semiconductors has the drawback that their strong intermolecular  $\pi$ - $\pi$  interactions induce thin-film dewetting, which results in non-uniform morphologies, and thus OTFTs based on these materials exhibit high device-to-device variation and their performance depends strongly on processing conditions.<sup>[7]</sup> In attempts to solve these problems, solution-processed small molecular semiconductors have been blended with polymers with excellent film-forming properties, and OTFTs based on such blend films have been fabricated.<sup>[8,9]</sup>

However, the resulting improvement in the performance of devices based on blend films is limited by the lateral phase separation of the blend films. Charge carriers are mostly transported in TFTs in a direction parallel to the substrate, so the formation of a vertically phase-separated bilayer structure is very important. However, a vertically phase-separated bilayer structure is difficult to attain in small molecular semiconductor/polymer blends mainly due to the lack of fine phase-separation control. Many factors (i.e., the surface tension of each component, the solvent evaporation rate, and the condition of the substrate) affect the phase separation, so tuning these properties is necessary for the fabrication of a phase-separated bilayer structure, as has already been successfully demonstrated in semiconducting polymer/insulating polymer blends.<sup>[10,11]</sup> We recently fabricated a triethylsilylethynyl anthradithiophene (TES-ADT) (top)/poly(methyl methacrylate) (PMMA) (bottom) bilayer structure by spin-casting the blend solution, performing solvent-vapor annealing, and then utilizing the phase-separated interface between TES-ADT and PMMA as the active channel.<sup>[12]</sup> However, a two-step process involving both spin-casting and solvent-vapor annealing was used in the fabrication of this bilayer structure. If a bilayer structure can be fabricated with one-step spin-casting and the resulting phase-separated interface is precisely controlled, then blending a small molecular semiconductor with an insulating

Dr. W. H. Lee, D. Kwak, H. H. Choi, S. G. Lee, Prof. K. Cho  
Department of Chemical Engineering  
Pohang University of Science and Technology  
Pohang, 790-784, Korea  
E-mail: kwcho@postech.ac.kr

Prof. J. E. Anthony  
Department of Chemistry  
University of Kentucky  
Lexington, 40506, USA

Prof. H. S. Lee  
Department of Chemical Engineering  
Hanbat National University  
Daejeon, 305-719, Korea

Dr. D. H. Kim  
Display Device & Materials Laboratory  
Samsung Advanced Institute of Technology  
Yongin, 446-712, Korea

DOI: 10.1002/adfm.201101159



polymer would become a promising technology for the fabrication of high performance OFETs.

In the present study, difluorinated-triethylsilylethynyl anthra-dithiophene (F-TESADT), which has previously been shown to exhibit a high field-effect mobility,<sup>[5,13,14]</sup> was used as the small molecular semiconductor. We investigated the film forming properties of F-TESADT and the usefulness of a binding polymer in the preparation of uniform F-TESADT films. Further, the dependence on the solvent evaporation rate of the formation of a bilayer structure from F-TESADT/insulating polymer blends and of the development of a phase-separated interface were investigated. Finally, the utilization of these blend films in the fabrication of OTFTs was tested.

## 2. Experimental Details

### 2.1. Materials and Sample Preparation

F-TESADT was synthesized following the procedure reported by Anthony and coworkers.<sup>[5]</sup> PMMA ( $M_w = 996 \text{ kg mol}^{-1}$ ), polystyrene (PS) ( $M_w = 350 \text{ kg mol}^{-1}$ ), toluene, chlorobenzene, 1,2-dichlorobenzene, 1,2,4-trichlorobenzene, octane and cyclohexane were purchased from Aldrich Chemical Co. Heavily doped n-type silicon substrates (containing a 300 nm thick thermally grown  $\text{SiO}_2$  layer) were cleaned in piranha solution, washed with distilled water, and stored in a vacuum oven prior to use. F-TESADT solution (10 mg mL<sup>-1</sup>) in chlorobenzene, F-TESADT/PMMA (1:1 w/w) blend solutions (20 mg mL<sup>-1</sup>) in toluene, chlorobenzene, 1,2-dichlorobenzene, and 1,2,4-trichlorobenzene and F-TESADT/PS (1:1 w/w) blend solutions (20 mg mL<sup>-1</sup>) in chlorobenzene and 1,2-dichlorobenzene were spin-cast onto the silicon substrate (at approximately 1500 rpm). The physical properties of the solvents used in this study are shown in **Table 1**. After spin-casting, the samples were transferred to a vacuum oven and left overnight to remove the residual solvent. For the top-contact TFTs, Au source-drain electrodes (channel length: 50  $\mu\text{m}$ , width: 800  $\mu\text{m}$ ) were thermally evaporated through shadow masks. For selective removal of the F-TESADT layers, the as-cast F-TESADT/PMMA blend films were etched with cyclohexane whereas the as-cast F-TESADT/PS blend films were etched with octane.

### 2.2. Characterization

The film morphologies were characterized by using an optical microscope (Zeiss), field-emission scanning electron microscopes

**Table 1.** Physical properties of the solvents at room temperature (27 °C). Data compiled from the “Chemical Properties Handbook.”<sup>[15]</sup>

	Boiling point [°C]	Vapor pressure [kPa]	Surface tension [dyn cm <sup>-1</sup> ]	Solubility parameter [cal <sup>1/2</sup> cm <sup>-2</sup> /3]
Toluene	110.6	4.2	27.9	8.9
Chlorobenzene	131.7	1.8	32.9	9.4
1,2-Dichlorobenzene	180.5	0.2	36.6	9.9
1,2,4-Trichlorobenzene	214.4	0.06	44.7	10.1

(Hitachi S-4200 and JEOL JSM-7401F), and an atomic force microscope (Digital Instruments Multimode) operating in tapping mode. Film thickness was determined by using a surface profiler (AlphaStep 500). The elemental compositions of the film were obtained by using energy dispersive X-ray spectroscopy (EDS) in conjunction with field-emission scanning electron microscopy (FESEM). X-ray photoelectron spectra were recorded on a VG ESCALAB 220i spectrometer with a Mg K $\alpha$  X-ray line (1253.6 eV), which was operated at 15 kV and 20 mA. Depth profiles were obtained by etching the films with an Ar<sup>+</sup> gun (3.0 kV). Out-of-plane/in-plane X-ray diffraction (XRD) and two-dimensional grazing-incidence X-ray diffraction (2D-GIXD) measurements were performed at the 10C1 and 4C2 beamlines at the Pohang Accelerator Laboratory in Korea to study the crystal orientations in the films. The capacitance was determined by using an Agilent 4284 precision LCR meter, and Keithley 236, 2400, and 4200-SCS source/measure units were employed to study the current–voltage characteristics of the devices under ambient conditions.

## 3. Results and Discussion

### 3.1. Film Formation Characteristics of F-TESADT

To investigate the morphologies of F-TESADT films, a F-TESADT solution with a concentration of 10 mg mL<sup>-1</sup> in chlorobenzene (CB) was spin-cast onto a silicon wafer (see **Figure 1a** for the chemical structure of F-TESADT). F–F and F–S interactions between F-TESADT molecules are known to impart fast crystallization, so spin-cast F-TESADT films have a crystalline structure.<sup>[5]</sup> However, the grain size of crystals is very small (see inset, **Figure 1b**) and the film does not completely cover the substrate (**Figure 1c**). The energy dispersive X-ray spectroscopy (EDS) spectra in **Figure S1** (see the Supporting Information) confirm that the region between the F-TESADT crystals is  $\text{SiO}_2$  and thus some of the F-TESADT crystals have dewetted from the  $\text{SiO}_2$  substrate. Top-contact transistors using F-TESADT films as the active layers exhibit low field-effect mobilities of approximately 10<sup>-3</sup> cm<sup>2</sup> V<sup>-1</sup> s<sup>-1</sup>; the reduction in the drain current at high  $V_G$  is possibly due to the dewetting of the F-TESADT films and charge trapping between silanol groups on  $\text{SiO}_2$  and F-TESADT molecules (**Figure 1d**).<sup>[16]</sup> To enhance the field-effect mobility of transistors based on F-TESADT films, a processing method for fabricating highly crystalline F-TESADT films with large grain size and good coverage is required.

To increase the grain size of F-TESADT crystals, a contact-induced crystallization method has been developed and it was found to be possible to obtain F-TESADT crystals with a large grain size and preferential orientation on chemically modified source/drain electrodes.<sup>[13]</sup> In this method, strong substrate–molecule interactions are vital to increase the grain size of the crystals. It is generally accepted that the molecular ordering of conjugated molecules can be increased by using a solvent with a high boiling point (or low vapor pressure). However, when a solvent with a high boiling point (i.e., 1,2-dichlorobenzene (DCB)) is used, the F-TESADT film is severely dewetted from the substrate and no inter-connected crystals were formed (see **Figure S2a**). The complete wetting of F-TESADT solutions (a contact angle

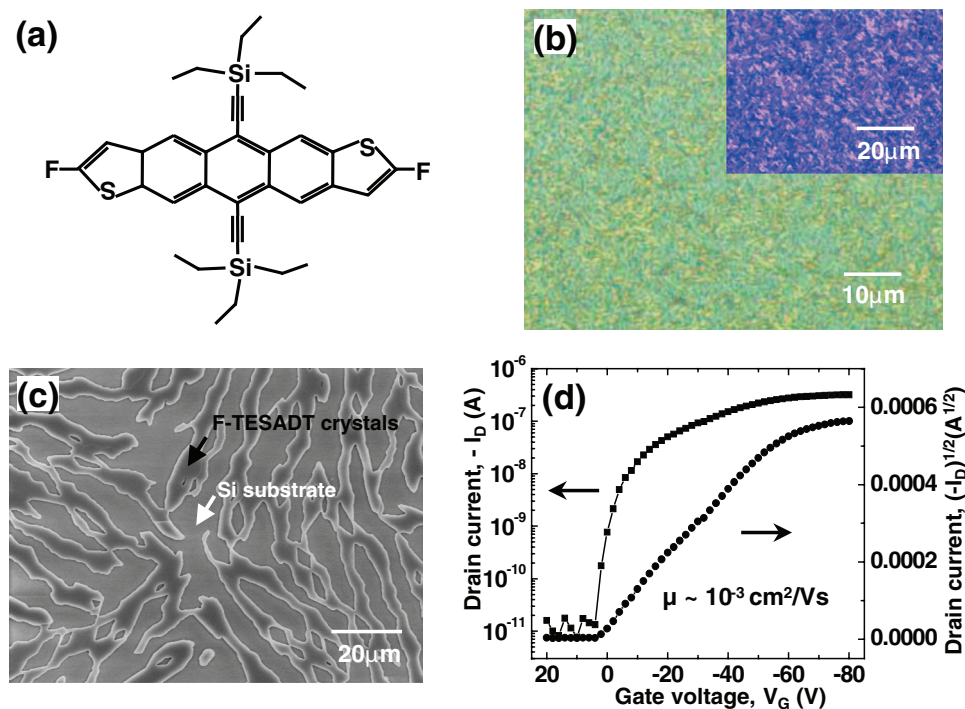


**Figure 1.** a) Chemical structure of difluorinated-triethylsilylethynyl anthradithiophene (F-TESADT). b) Optical microscopy (OM), and, c) field emission scanning electron microscopy (FESEM) images of F-TESADT films spin-cast from chlorobenzene solution. d) Transfer characteristics of the TFT device based on the F-TESADT film in (c). Drain voltage ( $V_D$ ) is fixed at  $-80$  V. The inset in (b) shows the polarized OM image.

below  $10^\circ$  regardless of the solvent) has been observed on silicon substrates, so the dewetting of the film is not due to the typical wetting problems of hydrophobic substrates, as previ-

ously reported.<sup>[17]</sup> Instead, the formation of F-TESADT films is possibly governed by kinetic limitations during spin-casting, as illustrated below. When DCB is used, the time required for solidification increases (approximately 18 s) over that for CB (approximately 5 s). The formation of a F-TESADT film is not possible for such a low solvent evaporation rate. Thus, a binding material is necessary and in this work, PMMA, which is an insulating polymer with good film-forming characteristics as shown in Figure S2b, was used. PMMA contains carbonyl groups, which interact strongly with silanol groups on silicon substrates.<sup>[18]</sup> PMMA is an appropriate binding material for spin-casting because the formation of F-TESADT thin films is possible in the presence of PMMA even at a low solvent evaporation rate.

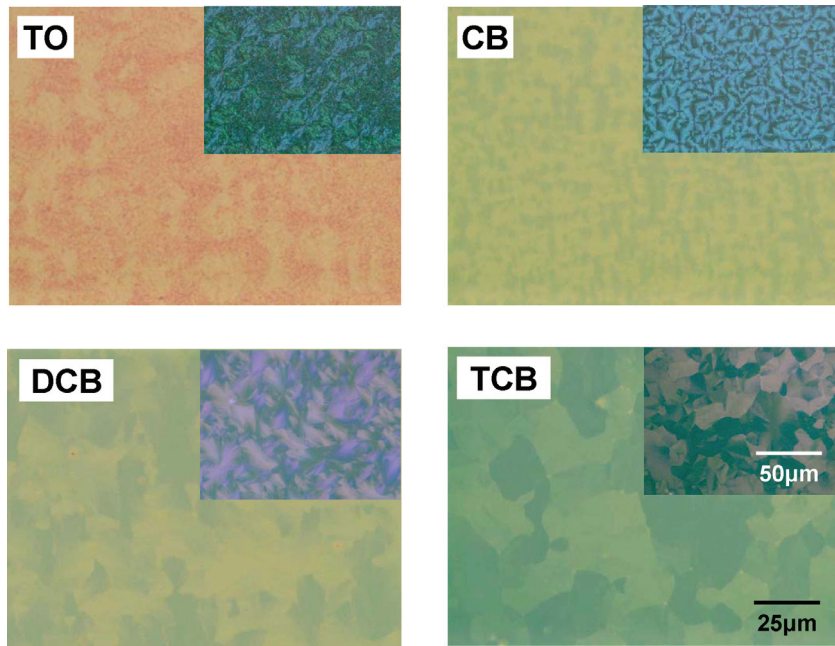


**Figure 2.** OM images of F-TESADT/PMMA blend films spin-cast from various solvents (TO: toluene, CB: chlorobenzene, DCB: 1,2-dichlorobenzene, TCB: 1,2,4-trichlorobenzene). The insets show the polarized OM images.

OM images of F-TESADT/PMMA (1:1) blend films spin-cast from various solvents. PMMA binds strongly with the silanol group on the silicon substrate,<sup>[18]</sup> so uniform blend films were obtained even when prepared with high boiling point solvents (DCB and 1,2,4-trichlorobenzene (TCB)). When low boiling point solvents (toluene (TO) and CB) are used, the grain sizes of the F-TESADT crystals are small, as shown in the polarized OM images (Figure 2). These results imply that the rapid solidification and crystallization of F-TESADT molecules reduce the  $\pi$ - $\pi$  interactions along the lateral direction due to the fast evaporation of these solvents. The grain sizes of the F-TESADT crystals in the F-TESADT/PMMA blend films increase with increases in the boiling point (or decreases in the vapor pressure, see Table 1) of the solvent. F-TESADT crystals with sizes of several tens of micrometers are observed when DCB or TCB is used. It is well known that solvent evaporation rate in spin-cast blend solution is complex interplay between solvent and components and is determined by type of components, solvent and concentration of each component. To simply this complex behavior, it is supposed that the solvent evaporation rate is proportional to vapor pressure of the solvent. Because we used exactly the same amount of F-TESADT and PMMA for

making F-TESADT/PMMA blend solution at each solvent (TO, CB, DCB, TCB), it is reasonable that solvent evaporation rate is dominantly determined by vapor pressure of each solvent.

To characterize the phase-separations of the blend films, AFM images were obtained and these are shown in Figure 3. Phase-separated structures composed of F-TESADT and PMMA can be clearly seen in the phase images. In the blend film spin-cast from CB, discrete crystals of F-TESADT with heights of around 80 nm are present at the air-film interface. The granular phase structure in the AFM image and the EDS spectra in Figure S3 confirm that the region between the F-TESADT crystals is PMMA. Thus, we conclude that dewetting occurs in the blend film between F-TESADT and PMMA. In the blend film spin-cast from DCB, the thickness of the F-TESADT crystals at the air-film interface is approximately 25 nm and a much more continuous F-TESADT film is obtained at the air-film interface. To investigate the vertical composition of the blend films, the depth profile of the DCB blend film was obtained by using X-ray photoelectron spectroscopy (XPS) combined with argon sputtering (Figure 4). Only the F-TESADT contains sulfur and fluorine atoms, so the variations with sputter depth in the sulfur and fluorine signals were monitored. At the region close

to the surface (0 to 15 min), sharp sulfur and fluorine signals, which are due to F-TESADT molecules, are detected. For 20 to 40 min, the sulfur and fluorine signals weaken abruptly, while the carbon signal strengthens a little, which implies that the underlying PMMA layer is detected. The AFM and XPS results show that a F-TESADT (top)/PMMA (bottom) vertically phase-separated bilayer structure forms during spin-casting.

To further characterize phase-separated morphologies of the F-TESADT/PMMA blend films, field emission scanning electron microscopy (FESEM) images were obtained (Figure 5). In the blend films spin-cast from TO and CB, phase-separated structures can be seen in the lateral and vertical direction. These structures consist of co-continuous regions of F-TESADT and PMMA, which proves that spinodal decomposition might be dominant mechanism for the phase separation. This kind of demixing and phase separation is formed when the phase mixture crosses the phase boundary into the unstable region.<sup>[20]</sup> In the blend films spin-cast from DCB and TCB, the F-TESADT crystals cover large parts of the air-film interface. The time required to thin the transient wetting layer during spin-casting increases with increases in the boiling point of the solvent (or decreases in the solvent vapor pressure), so F-TESADT molecules become effectively phase-separated from PMMA and the F-TESADT crystals can grow, which results in an increase in the crystal coverage. A difference in solubility is also known to contribute to vertical phase separation. In our

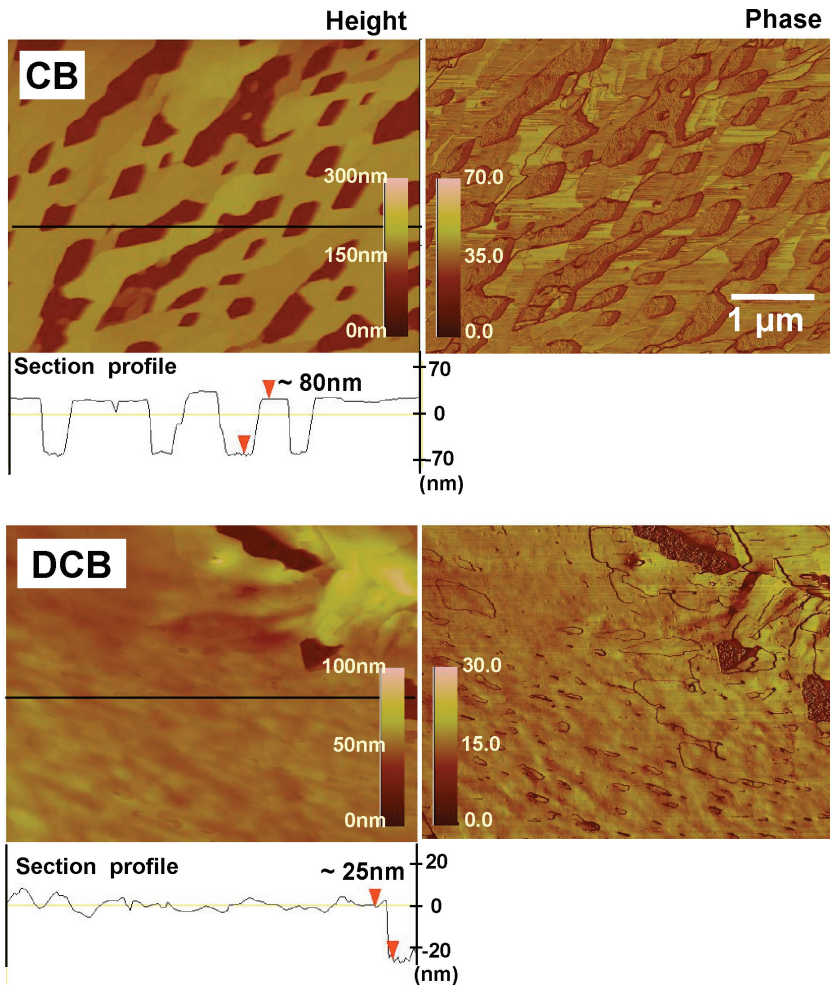
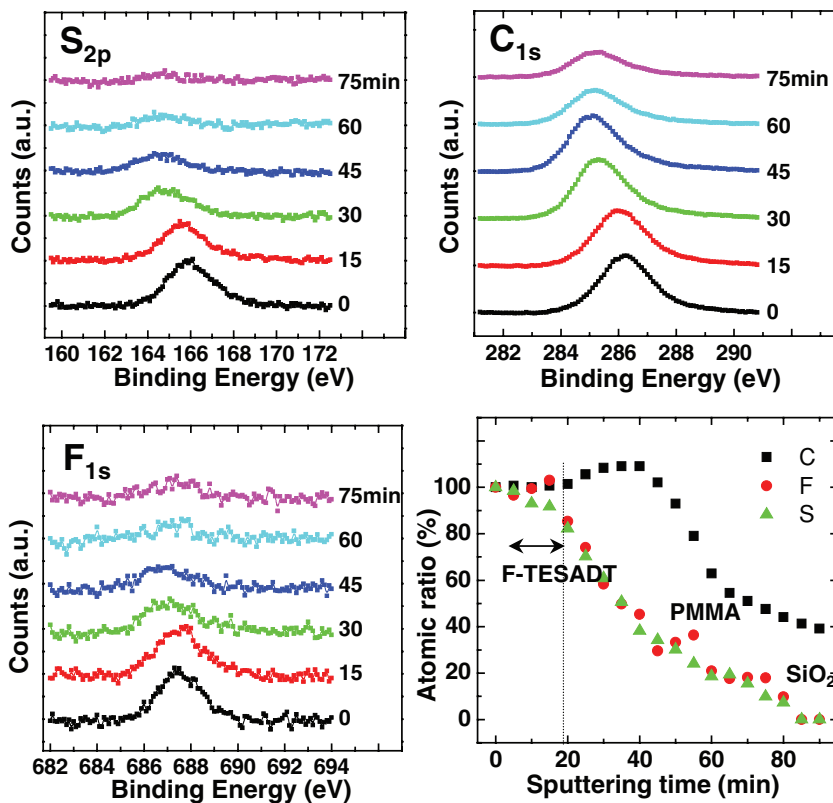


Figure 3. Atomic force microscopy (AFM) images of F-TESADT/PMMA blend films spin-cast from the solvents CB and DCB.



**Figure 4.** Variation with sputter time of the X-ray photoemission spectrum ( $S_{2p}$ ,  $C_{1s}$ , and  $F_{1s}$ ) of a F-TESADT/PMMA blend film spin-cast from DCB and the relative ratios of sulfur, carbon, and fluorine atoms as a function of the sputter time.

study, however, the difference between the solubility parameters from solvent to solvent is much smaller than that between the solvent vapor pressures (see Table 1) and thus the solvent evaporation rate is the dominant influence on the phase-separation characteristics of the F-TESADT/PMMA blend films. Although the final film thicknesses are significantly different, the bilayer structures in the cross-section images of the blend films spin-cast from DCB and TCB can be clearly seen in the insets in Figure 5. This vertical phase separation is mainly due to the difference between the surface energies of F-TESADT and PMMA. The water contact angle of the F-TESADT film is  $106^\circ$ , which is much higher than that of PMMA ( $74^\circ$ ). After the more polar PMMA component of the F-TESADT/PMMA blends is preferentially adsorbed onto the hydrophilic silicon substrate, the F-TESADT molecules solidify and crystallize on PMMA layer. Furthermore, because F-TESADT is highly crystalline, the tendency to phase separate is enhanced by the enthalpic interaction during crystallization.<sup>[11]</sup> A large proportion of the F-TESADT molecules in PMMA move toward the air-film interface due to the enthalpic force of

during spin-casting and the subsequent fast-crystallization of F-TESADT molecules at the air-film interface might increase

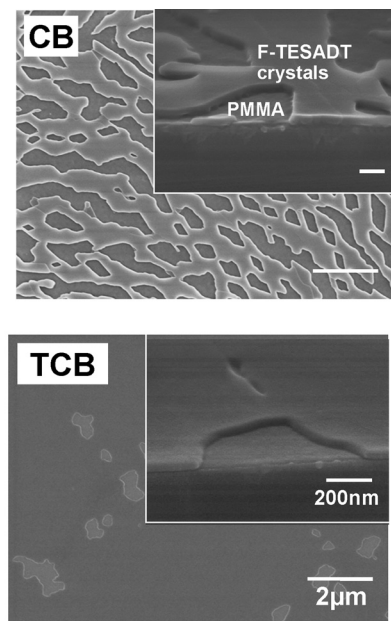


**Figure 5.** Field-emission scanning electron microscopy (FESEM) images of F-TESADT/PMMA blend films spin-cast from various solvents (TO, CB, DCB, TCB). The insets show the cross-sectional images.

crystallization in addition to the surface energy difference, so vertical phase separation is enhanced.

It is known that the interface between the semiconductor and the dielectric critically affects the electrical properties of TFTs.<sup>[21]</sup> To elucidate the characteristics of the interface between F-TESADT and PMMA, the preferentially segregated F-TESADT layers were selectively removed by etching the films with cyclohexane, which does not dissolve PMMA. The surface morphologies, which correspond to the morphologies of the interfaces between F-TESADT and PMMA, were characterized with AFM (Figure 6) and two-dimensional power spectra density (PSD) graphs were calculated by squaring the Fourier transforms of the AFM height images (Figure 7). PSD is a powerful tool because it can reveal multiscale surface features including spatial modulations.<sup>[22]</sup> In the blend film spin-cast from TO, a rough film with a root mean square (RMS) roughness of approximately 15 nm and some holes with depths of 80–90 nm (equal to the thickness of the PMMA layer) were observed. Furthermore, the characteristic wavelength of approximately 400 nm in the PSD graph coincides with the lateral domains observed in the AFM images (Figure 6, TO). The available time for phase separation is not sufficient for the blend film spin-cast from TO, so some F-TESADT molecules remain in PMMA

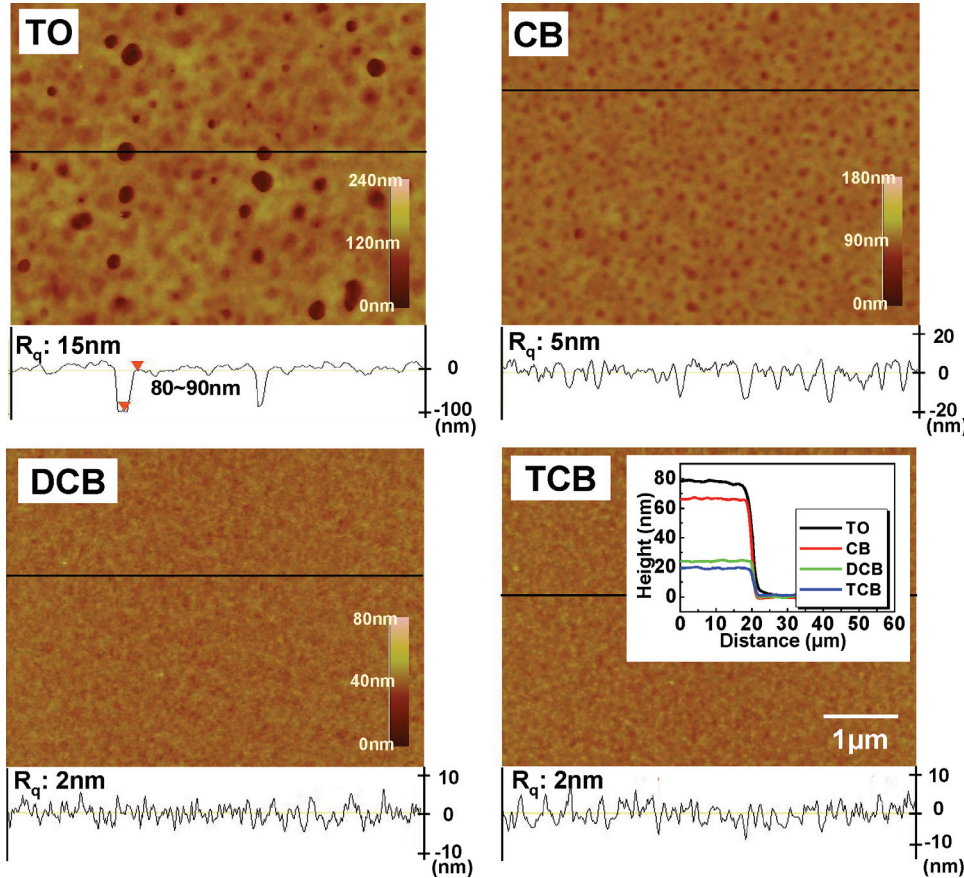


**Figure 6.** AFM images of the cyclohexane-etched F-TESADT/PMMA blend films spin-cast from various solvents. The inset in the TCB image shows the surface profiles of the cross-sections of the cyclohexane-etched F-TESADT/PMMA blend films spin-cast from various solvents.

the roughness of the interface and trigger hole formation in the PMMA layer. Holes are also observed when the homo-PMMA solution in TO is spin-cast (see Figure S4). However, these holes are of much lower depth (around 10 nm) than those of the blend films, which indicates that the evolution of roughness in the blend film is dominated by phase separation. In the blend film spin-cast from CB, the RMS roughness is 5 nm, but spatial modulations of the wavelength near 200 nm in the AFM image and the PSD graph are still observed. As the boiling point of the solvent increases (or the vapor pressure of the solvent decreases) further, the interface becomes much smoother, and a RMS roughness of 2 nm is reached in the blend films spin-cast from DCB and TCB. These roughness values are higher than those of spin-cast homo-PMMA films (0.2 to 0.8 nm depending on the solvent used, see Figure 6 and S4). However, an abrupt interface between F-TESADT and PMMA is achieved through fine control of the solvent evaporation rate by using high boiling point solvents.

### 3.3. Phase-Separation Characteristics of F-TESADT/PS Blends

To demonstrate the feasibility of other polymers for the use of binding materials, PS was blended with F-TESADT and the

blend solution was spin-cast on  $\text{SiO}_2/\text{Si}$  substrate. As discussed above, the surface energy of the binding polymer should be high enough for F-TESADT molecules to segregate and crystallize at the air-film interface. The water contact angle of the PS film is measured to be  $86^\circ$ , much lower than that of F-TESADT ( $106^\circ$ ). Thus, PS is expected to be suitable for the counterpart polymer in the context of phase-separation with F-TESADT. We used two different solvents (CB and DCB) to examine the phase-separation characteristics of F-TESADT/PS blends. However, when a DCB was used, no continuous F-TESADT/PS blend film formed. This differs from the results in F-TESADT/PMMA blend films, which exhibit uniform morphologies in the samples of DCB and TCB (Figure 2 and Figure 5). These differences in film-forming properties prove that PMMA is much better than PS as a binding material for F-TESADT because PMMA contains the carbonyl group which is known to bind strongly with the silanol group on the silicon substrate. On the other hand, PS does not contain such functional groups.

and thus the use of solvent with a high boiling point results in dewetting of the blend films during the spin-casting process.

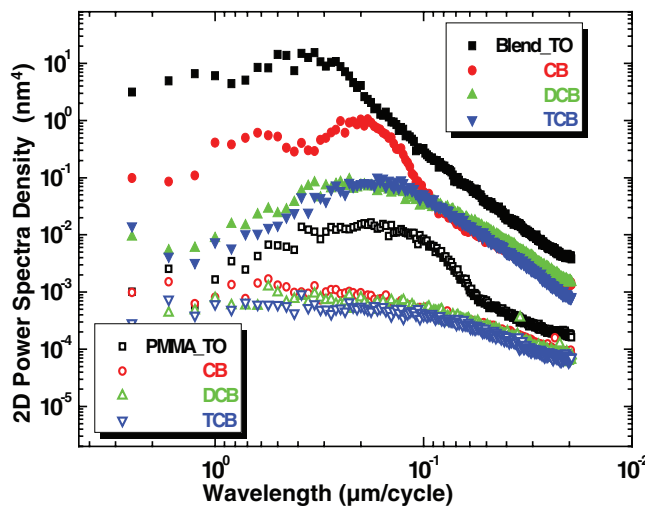


**Figure 7.** Two-dimensional power spectra density (PSD) graphs of the cyclohexane-etched F-TESADT/PMMA blend films (Figure 6) and PMMA films (Figure S4).

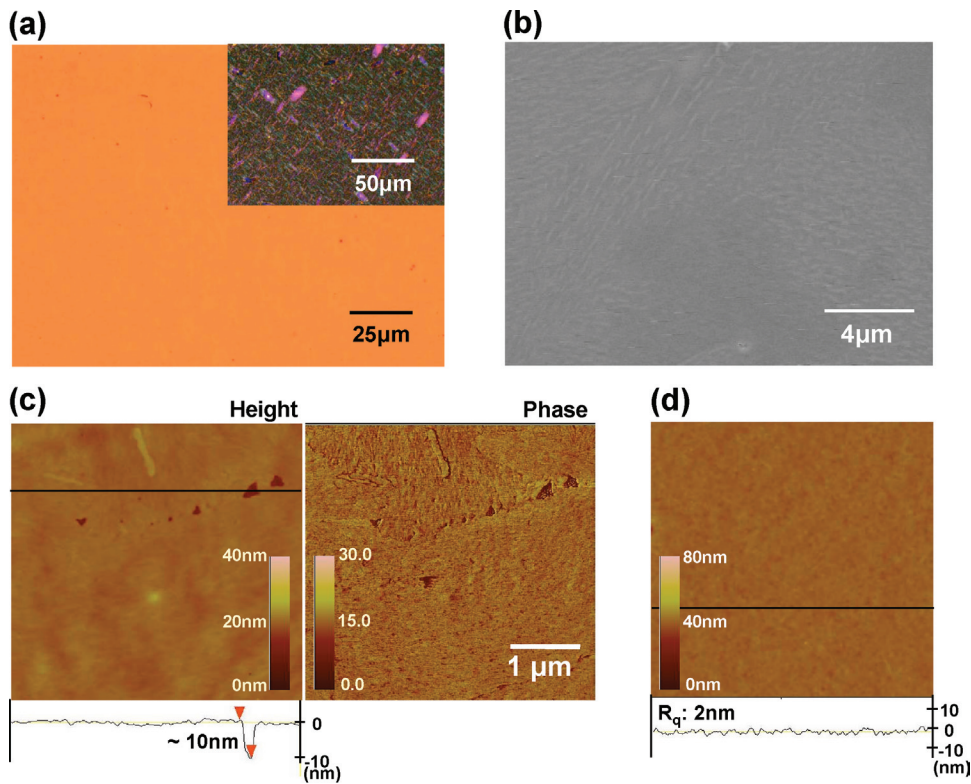


**Figure 8.** OM (a), FESEM (b), and AFM (c) images of F-TESADT/PS blend films spin-cast from CB. The inset in (a) shows the polarized OM image. d) AFM image of the octane-etched F-TESADT/PS blend film spin-cast from CB.

When CB was used as a solvent for preparing F-TESADT/PS blend solution, uniform blend film formed on the silicon substrate. Figure 8a and b show morphological and structural characteristics of F-TESADT/PS blend films proved by OM and FESEM, respectively. The polarized OM and FESEM images show that small F-TESADT crystals have formed. To investigate whether these crystals were placed at the air-film interface, the surface morphology of the blend film was characterized with an AFM (Figure 8c). This image resembles the surface morphology of a F-TESADT/PMMA blend film spin-cast from DCB (Figure 3). Comparing height and phase images, it can be deduced that F-TESADT crystals cover a larger part of the air-film interface, and the thickness of the F-TESADT layer is around 10 nm (as confirmed by section profile). On the other hand, the region which is not covered by F-TESADT crystals might be underlying PS, which is phase-separated and solidified first during the spin-casting process. To support this idea, the preferentially segregated F-TESADT layer was selectively removed by etching the blend film with octane which does not dissolve PS. As a result, the AFM image of Figure 8d reveals that the underlying PS surface is quite smooth (RMS roughness around 2 nm). All of these observations confirm that a bilayer structure containing F-TESADT crystals on the top and PS on the bottom can also be fabricated by spin-casting F-TESADT/PS blend solution in a one-step process. To conclude, PS can also be used as binding materials for F-TESADT if the boiling point of the used solvent is carefully selected.

### 3.4. Crystalline Structures of F-TESADT in the F-TESADT Film and the F-TESADT/PMMA Blend Films

To determine the inner structures of the F-TESADT film and the F-TESADT/PMMA blend films, X-ray diffraction (XRD) patterns were obtained and are shown in Figure 9. Figure 9a shows the out-of-plane and in-plane XRD patterns with the molecular axis in the inset. The out-of-plane XRD patterns contain (00l) diffraction peaks for all the films, and thus the F-TESADT molecules stack with silyl groups on the substrate surface.<sup>[13]</sup> The in-plane XRD patterns contain (l00) and (0l0) diffraction peaks. In addition, (001) diffraction peaks are present in the patterns of the F-TESADT film and the F-TESADT/PMMA blend films spin-cast from TO and CB, which implies that these films contain both standing-up and lying-down molecules (see Figure S5). In contrast, (001) diffraction peaks are absent in the in-plane XRD patterns of the F-TESADT/PMMA blend films from DCB and TCB, and thus the standing-up style molecular orientation is dominant in those films.

We further investigated the molecular orientations in the F-TESADT film and the F-TESADT/PMMA blend films with two-dimensional grazing incidence XRD, as shown in Figure 9b. The F-TESADT film produces (00l) diffraction peaks at  $q_{xy} = 0$  and many reflection spots along  $q_z$  for a given  $q_{xy}$ , which can be indexed as a combination of (100) and (010) diffractions. Furthermore, the (001) diffraction peak for the azimuthal angle direction shows not only that the crystals are well-oriented along  $q_z$  (standing-up) but also that there are misoriented crystals

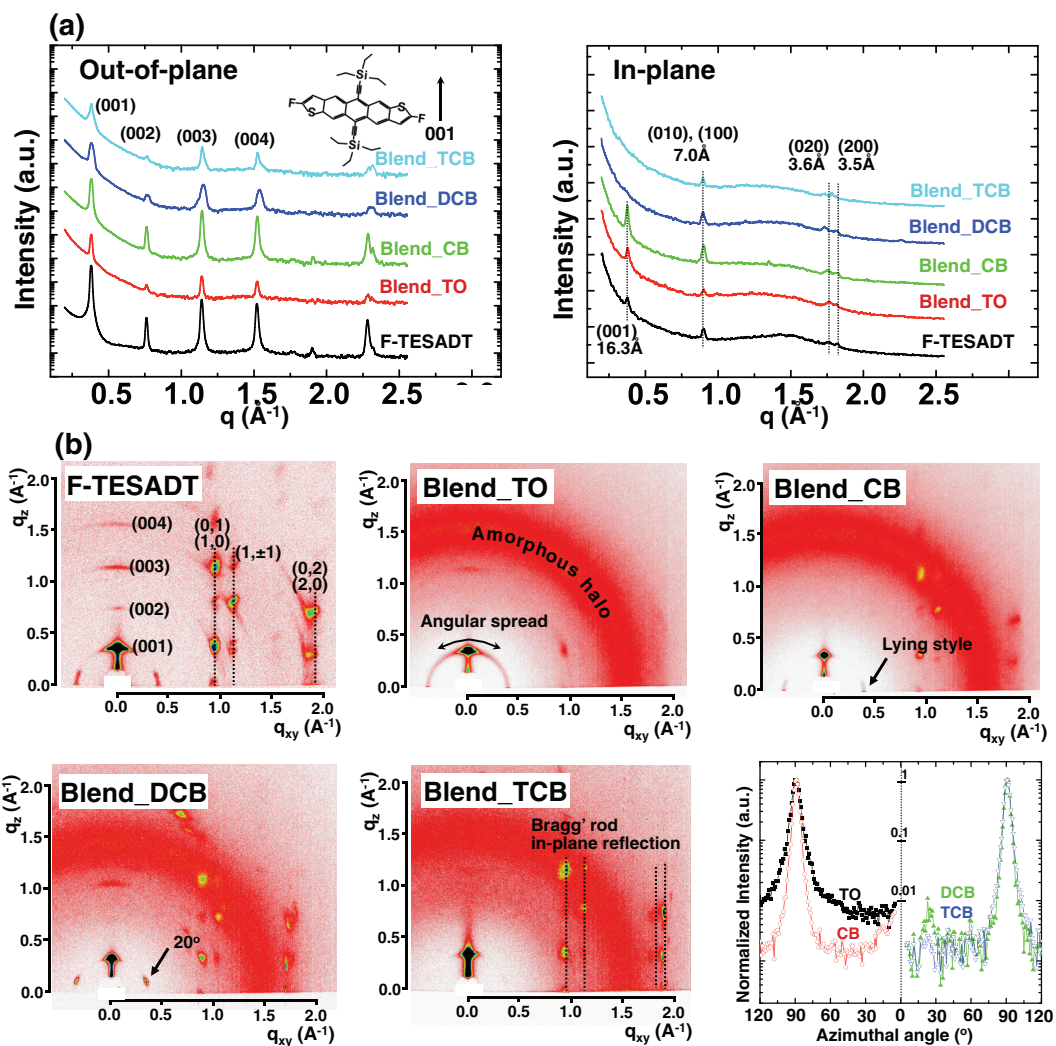


**Figure 9.** a) Out-of-plane (left) and in-plane (right) X-ray diffraction patterns for the F-TESADT film (F-TESADT) and the F-TESADT/PMMA blend films spin-cast from various solvents (Blend\_TO: toluene, Blend\_CB: chlorobenzene, Blend\_DCB: 1,2-dichlorobenzene, Blend\_TCB: 1,2,4-trichlorobenzene). The inset shows the molecular axis of F-TESADT. b) Two-dimensional grazing incidence X-ray diffraction (2D GIXD) patterns for the F-TESADT film and the F-TESADT/PMMA blend films spin-cast from various solvents. Azimuthal angle scans at  $q_{(001)}$  from the 2D GIXD patterns of the F-TESADT/PMMA blend films are also shown.

along  $q_{xy}$  (lying-down), which is in agreement with a previous report.<sup>[13]</sup> In F-TESADT/PMMA blend films, the F-TESADT molecules are phase-separated from PMMA and segregate at the air-film interface, thus the diffraction patterns of the blend films are characteristic of the F-TESADT molecular orientation on PMMA. In the blend film spin-cast from TO, we can observe the broad angular spread of the (001) diffraction peak and the vague in-plane reflections. This solvent evaporates rapidly, so the F-TESADT molecules are not perfectly phase separated and thus the crystallization of the F-TESADT molecules is hindered by PMMA segments. Note that the diffraction pattern of the F-TESADT film spin-cast from the same solvent (i.e., TO) contains highly ordered in-plane reflections, which are not present in that of the blend film (see Figure S6). The in-plane reflection spots of the blend film spin-cast from CB are much more intense than those of the blend film spin-cast from TO, which

suggests that the lateral assembly of F-TESADT molecules is enhanced by using a solvent with a high boiling point (or a low vapor pressure). For the blend films spin-cast from DCB and TCB, the diffraction patterns contain many reflection spots along  $q_z$  at a given  $q_{xy}$ , which suggests that F-TESADT molecules adopt three-dimensional multi-layered structures. The variation in the molecular orientation in the blend films with the solvent properties is evident when the azimuthal angle scans at  $q_{(001)}$  are compared (Figure 9b). Each curve was normalized by the maximum of the (001) peak along  $q_z$ . As the boiling point of the solvent increases (or the vapor pressure decreases), the full-width-at-half-maximum (FWHM) decreases, which indicates that crystal perfection with standing-up molecular orientation is improved. Whereas only the standing-up molecular orientation was obtained in the blend film spin-cast from TCB, very small portions of the lying-down and tilted ( $20^{\circ}$  with respect

to the surface normal) orientation were detected in the blend films spin-cast from CB and DCB, respectively. We speculate that the occurrence of the 20° tilted orientation, which was also observed in the F-TESADT film, might be related to the tilting of the fluorinated anthradithiophene backbone (see Figure S5). There are three possible molecular orientations of F-TESADT: standing-up, lying-down, and 20° tilted. The standing-up structure is energetically stable because its surface energy is the lowest. On the other hand, the lying-down and 20° tilted structures are kinetically stable. The anthradithiophene backbone has a tendency to lie down during spin-casting process due to the centrifugal force parallel to the surface. When the solvent evaporates rapidly, kinetically stable structures can occur despite the increase in surface energy.<sup>[23]</sup>

PMMA serves as an underlying binding material that prevents dewetting of F-TESADT from the substrate, so F-TESADT molecules can crystallize over sufficient time when there is slow evaporation of the solvent (i.e., TCB), which results in an energetically stable structure (i.e., standing-up). When homo F-TESADT is spin-cast, only a solvent with a low boiling point

(i.e., TO, CB) can be used because of the dewetting problem discussed above. As a consequence, the kinetically favored lying-down and 20° tilted orientations can also form, so the diffraction pattern of the homo F-TESADT film indicates the presence of mixed orientations. In the F-TESADT/PMMA blend film spin-cast from a low boiling point solvent, the crystallization of F-TESADT molecules is hindered by the time limitation on the phase-separation of the two components, which results in a film of F-TESADT with low crystallinity. In stark contrast, phase separation does not limit the crystallization of F-TESADT in the blend film spin-cast from a high boiling point solvent, and sufficient time for crystallization is ensured. As a result, F-TESADT crystals with large grain size and well-oriented structure are formed on PMMA. Furthermore, our approach using F-TESADT/PMMA blends provides a facile method for manipulating the molecular orientation of F-TESADT. By simply changing the solvent used in the blend solution, F-TESADT crystals with preferential orientation can be obtained on PMMA without the need for changes in other processing parameters such as substrate treatment. The morphological and structural variations of the F-TESADT/PMMA blends with the solvent boiling point (or vapor pressure) are shown schematically in Figure 10. By using high boiling point solvents, the time available for phase separation is significantly enhanced, which results in the formation of an abrupt interface between the two components and the growth of highly oriented F-TESADT crystals on the PMMA layer.

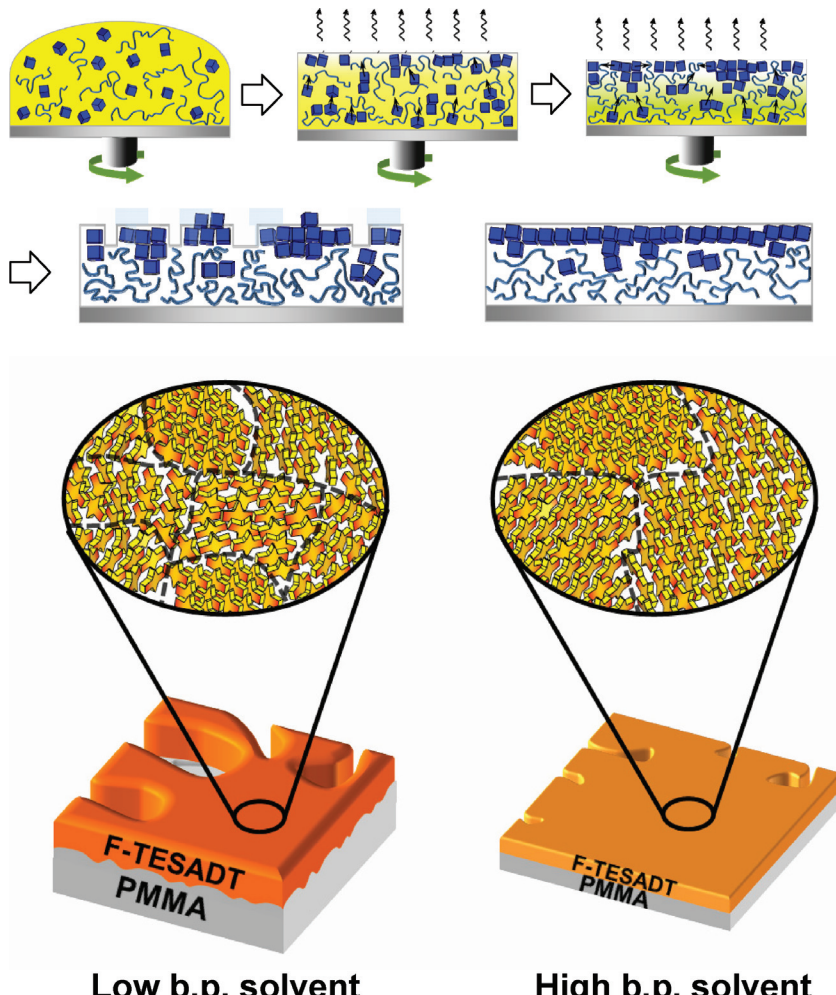


**Figure 10.** Schematic representations of the morphological and structural variations in the F-TESADT/PMMA blend films spin-cast from various solvents (left: low boiling point solvent, right: high boiling point solvent).

### 3.5. Electrical Properties of TFT Devices Based on F-TESADT/PMMA and F-TESADT/PS Blend Films

To evaluate the electrical characteristics of the F-TESADT/PMMA blend films, top-contact TFTs with Au electrodes were fabricated. The processing procedure is shown in Figure 11a. Phase-separated PMMA in the F-TESADT/PMMA blend films serves as the dielectric layer, so the dielectric consists of SiO<sub>2</sub> (300 nm) and PMMA and charges pass through the phase-separated interface between F-TESADT and PMMA. For this reason, not only the structure of F-TESADT molecules but also the characteristics of the interface between F-TESADT and PMMA can affect the electrical properties of TFTs based on F-TESADT/PMMA blend films. Figure 11b shows the output characteristics of TFTs based on blend films spin-cast from the various solvents. The saturation currents obtained from the output curves are ordered as follows: DCB ≈ TCB > CB > TO. The contact effect in the linear regime is the result of the limitations on charge injection, and is frequently observed for semiconductor films

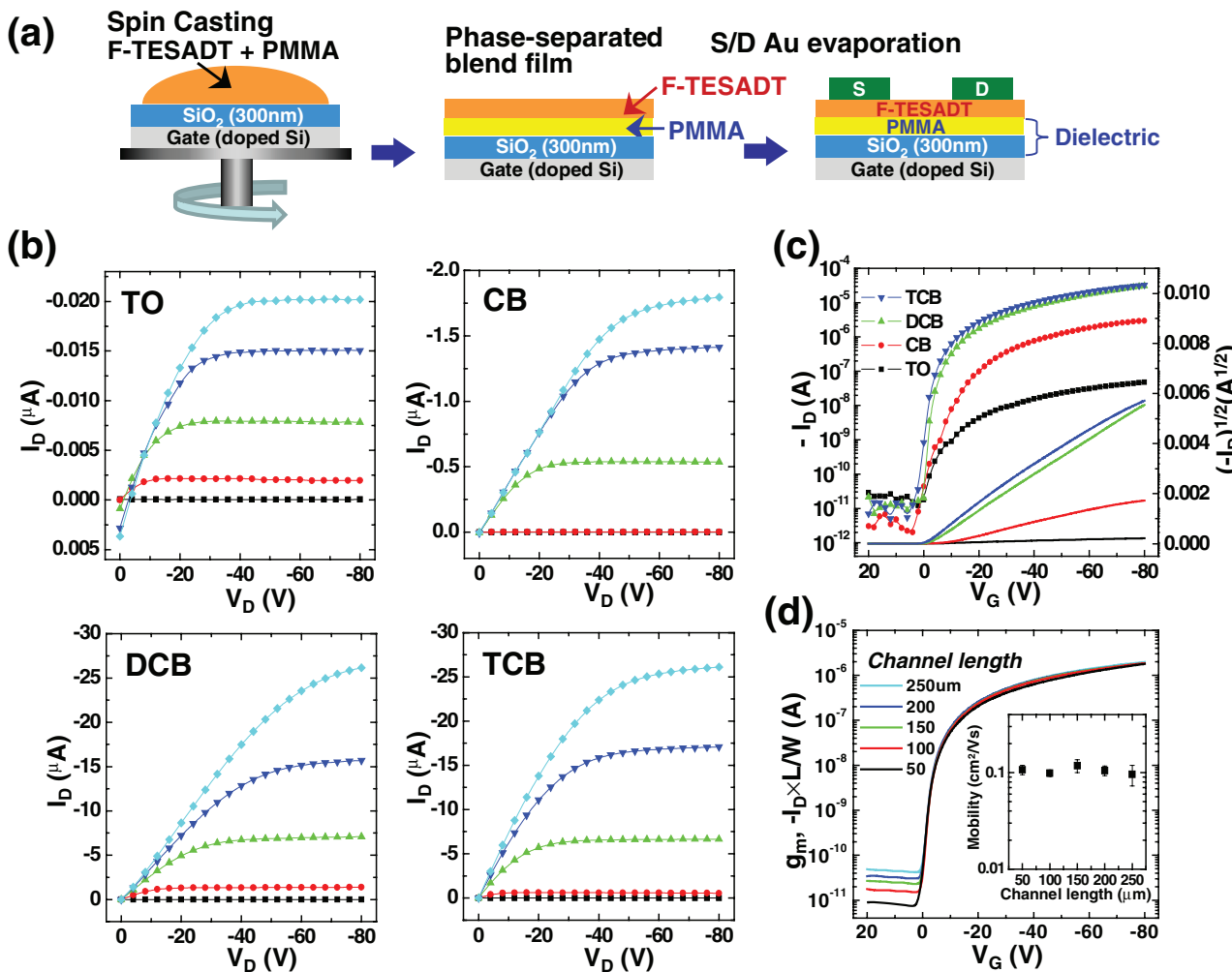


**Figure 11.** a) The processing procedure for the transistors based on F-TESADT/PMMA blend films. b) Output current–voltage characteristics of the transistors based on the F-TESADT/PMMA blend films spin-cast from various solvents (TO, CB, DCB, TCB). Gate voltage ( $V_G$ ) was changed from 0 V to –80 V with steps of –20 V. c)  $-I_D$  (left scale), and  $(-I_D)^{1/2}$  (right) versus  $V_G$  characteristics for the transistors based on F-TESADT/PMMA blend films spin-cast from various solvents.  $V_D$  was fixed at –80 V. d) Transconductance ( $g_m$ ) versus  $V_G$  characteristics of the transistors based on F-TESADT/PMMA blend films spin-cast from DCB with various channel lengths, where  $g_m$  is defined as  $(-I_D) \times L/W$ . The constant transconductances in the transfer curves mean that the field-effect mobility is independent of channel length. The inset shows the channel length dependent field-effect mobilities of the transistors based on F-TESADT/PMMA blend films spin-cast from DCB. The channel length was varied from 50 to 250  $\mu\text{m}$  for a fixed channel width (1000  $\mu\text{m}$ ) and the field-effect mobilities were calculated from the transfer characteristics in the saturation regime ( $V_D = -80$  V).

with a low-lying highest occupied molecular orbital (HOMO) level.<sup>[4,5]</sup> The HOMO level of F-TESADT is measured to be –5.46 eV (see Figure S7). Hole injection from Au electrode into F-TESADT is hampered and thus leads to a non-ohmic contact effect. Detailed device performance was assessed in the transfer characteristics and are shown in Figure 10c. Whereas the off-current levels remain constant (approximately  $10^{-11}$  A), the on-current level increases as the boiling point of the solvent increases (or as the vapor pressure decreases). Before extracting the field-effect mobilities from the transfer characteristics, the thickness and capacitance of the PMMA layer, which acts as the dielectric, were calculated and are shown in Table 2. The field-effect mobilities were calculated from the  $(-I_D)^{1/2}$  versus  $V_G$  characteristics of 10 to 20 devices (Table 3). The average field-effect mobilities, which were calculated using the total capacitance

of the dielectric including the PMMA layer, were found to be  $1.6 \times 10^{-4} \text{ cm}^2 \text{ V}^{-1} \text{ s}^{-1}$  (TO),  $1.2 \times 10^{-2} \text{ cm}^2 \text{ V}^{-1} \text{ s}^{-1}$  (CB),  $0.1 \text{ cm}^2 \text{ V}^{-1} \text{ s}^{-1}$  (DCB), and  $0.1 \text{ cm}^2 \text{ V}^{-1} \text{ s}^{-1}$  (TCB). The relatively low field-effect mobility of the TO device is mainly due to the small grain size of its F-TESADT crystals with low crystallinity (Figure 2 and 9). Grain boundaries and poorly oriented crystals disturb the  $\pi$ – $\pi$  interaction of F-TESADT molecules, which leads to obstacles of charge transport along in-plane direction. Because the device with TO blend film exhibits much lower field-effect mobility than that with F-TESADT film, there might be another limiting factor for low field-effect mobility in the device with TO blend film. It was observed that the grain sizes of F-TESADT crystals in TO blend film are not as small as those of crystals in F-TESADT film. We speculate that high RMS roughness of its interface between F-TESADT and PMMA (approximately 15 nm),

**Table 2.** Thickness and capacitance of the PMMA layers in etched F-TESADT/PMMA blend films spin-cast from various solvents.

	$t_{\text{PMMA}}^{\text{a)}$ [nm]	$C_{\text{PMMA}}^{\text{b)}$ [nF cm $^{-2}$ ]	$C_{\text{tot}}^{\text{b)}$ [nF cm $^{-2}$ ]
Toluene	80	31	8.0
Chlorobenzene	65	38	8.4
1,2-Dichlorobenzene	25	99	9.7
1,2,4-Trichlorobenzene	20	124	9.9

<sup>a)</sup>Obtained from the surface profiles of cross-sections of the cyclohexane-etched F-TESADT/PMMA blend films (see the inset in Figure 6b); <sup>b)</sup>Capacitances of PMMA ( $C_{\text{PMMA}}$ ) and the total dielectric ( $C_{\text{tot}}$ ) were calculated by using the following equations:  $C_{\text{PMMA}} = k\epsilon_0/t$ ,  $1/C_{\text{tot}} = 1/C_{\text{PMMA}} + 1/C_{\text{SiO}_2}$  (10.8 nF cm $^{-2}$ ), where the dielectric constant ( $k$ ) of PMMA is 2.8 and the permittivity of a vacuum ( $\epsilon_0$ ) is 8.85  $\times 10^{-14}$  F cm $^{-1}$ .

**Table 3.** Electrical properties of transistors based on the F-TESADT film, the F-TESADT/PS blend film, and the F-TESADT/PMMA blend films spin-cast from various solvents.

	$\mu$ [cm $^2$ V $^{-1}$ s $^{-1}$ ]	$I_{\text{on}}/I_{\text{off}}$	$V_{\text{th}}$ [V]
F-TESADT	$1.1 (\pm 0.5) \times 10^{-3}$	$\sim 10^5$	$9.6 (\pm 4.4)$
F-TESADT/PS <sup>a)</sup>	$7 (\pm 2) \times 10^{-3}$	$\sim 10^6$	$2.5 (\pm 4.5)$
F-TESADT/PMMA_TO	$1.6 (\pm 0.2) \times 10^{-4}$	$\sim 10^4$	$2.6 (\pm 2.3)$
F-TESADT/PMMA_CB	$1.2 (\pm 0.2) \times 10^{-2}$	$\sim 10^6$	$3.1 (\pm 1.1)$
F-TESADT/PMMA_DC	0.1 ( $\pm 0.02$ )	$\sim 10^7$	$1.3 (\pm 2.6)$
F-TESADT/PMMA_TCB	0.1 ( $\pm 0.03$ )	$\sim 10^7$	$0.4 (\pm 1.9)$

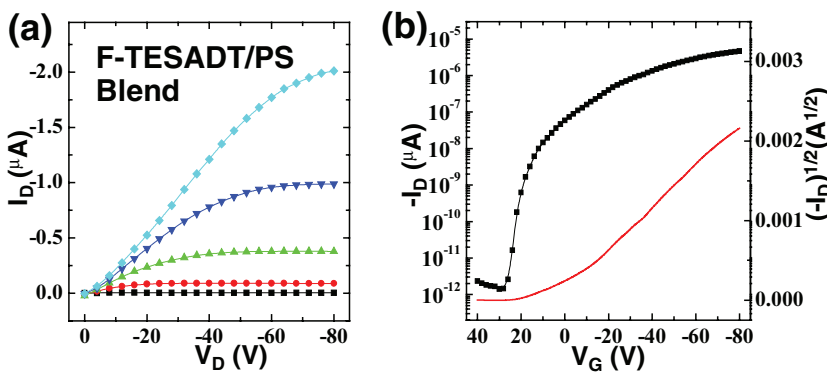
<sup>a)</sup>Obtained from FETs with F-TESADT/PS blend film spin-cast from CB. Capacitance of 8.7 nF cm $^{-2}$  was used for calculating field-effect mobility.

where accumulated charge carriers pass through, can be a dominant reason for the reduction of field-effect mobility. The higher field-effect mobility of the CB device is notable (around two orders of magnitude higher than that of the TO device). Aside from the lower roughness of its interface between F-TESADT and PMMA (15 nm (TO), 5 nm (CB)), the PSD graph of the CB film contains low spectral density for the wavelengths below 100 nm, which implies that the nanoscale roughness of the CB film is much lower than that of the TO film (Figure 7). In addition, the coverage/connectivity of the F-TESADT crystals of the CB film is higher than that of the TO film and the rod-like diffraction spots in the in-plane reflection indicate the possibility of two-dimensional charge transport. All these differences result in the high field-effect mobility of the CB device. The highest field-effect mobilities are those of the DCB and TCB devices, and are attributed to the formation of highly crystalline F-TESADT crystals with large grain size and high coverage on much smoother PMMA dielectrics. The standing-up molecular orientation of F-TESADT facilitates optimal  $\pi-\pi$  overlapping along the lateral direction, so the higher proportions of standing-up molecules in the DCB and TCB films enable fast charge

transport in the devices based on those films. The field-effect mobilities of the devices based on the blend films of DCB and TCB are much higher than that of the device based on homo F-TESADT (see Table 3). This improvement is directly due to the increases in the grain size of crystals, the coverage of crystals, and the crystalline order that result from the use of F-TESADT/PMMA blends in high boiling point solvents. The obtained field-effect mobilities are effective values and further increases can be possible by suitable electrode choice.

The highest value of the field-effect mobility obtained here is a little bit lower than that obtained in the contact-induced crystallization study of Gundlach et al., which reported a field-effect mobility of  $0.2 \text{ cm}^2 \text{ V}^{-1} \text{ s}^{-1}$  for a channel length of  $10 \mu\text{m}$ .<sup>[13]</sup> In that study, however, the field-effect mobility decreases with increasing channel length, falling to  $10^{-2}$  and  $10^{-3} \text{ cm}^2 \text{ V}^{-1} \text{ s}^{-1}$  for 50 and  $100 \mu\text{m}$ , respectively. In this study, the device based on a F-TESADT/PMMA blend film spin-cast from DCB exhibits field-effect mobilities ( $0.1 \text{ cm}^2 \text{ V}^{-1} \text{ s}^{-1}$ ) that are nearly independent of channel length, which indicates that the device performances are highly uniform (Figure 11d). Recently, F-TESADT was blended with polytriarylamine (PTAA) and was segregated at the air-film interface for the fabrication of top-gated TFTs.<sup>[9,14]</sup> TFTs based on F-TESADT/PTAA blend films exhibit a high off-current due to the high bulk current of the PTAA semiconducting polymer, which results in a low current on-off ratio (approximately  $10^4$ ). In contrast, PMMA is an insulating polymer and is fully phase-separated from F-TESADT, so the current on-off ratios of TFTs based on F-TESADT/PMMA blend films obtained in this study are high (around  $10^7$  for the DCB and TCB devices).

To compare the electrical characteristics of the F-TESADT/PS blend film with those of the F-TESADT/PMMA blend films, FETs based on the F-TESADT/PS blend film spin-cast from CB was measured (Figure 12). The output curve in Figure 12a shows well-behaved linear and saturation regimes, and the saturation current at each  $V_G$  is similar to that of FETs based on F-TESADT/PMMA blend film spin-cast from CB. The transfer characteristic was measured to extract field-effect mobility (Figure 12b). Because the PS layer, which is phase-separated on the bottom, also acts as the dielectric, the capacitance of the PS layer ( $44 \text{ nF cm}^{-2}$ ), which corresponds to a 50 nm thick film with a dielectric

**Figure 12.** a) Output current–voltage characteristic of the transistor based on the F-TESADT/PS blend film spin-cast from CB.  $V_G$  is changed from 0 to  $-80 \text{ V}$  with an interval of  $-20 \text{ V}$ . b)  $-I_D$  (left scale), and  $(-I_D)^{1/2}$  (right) versus  $V_G$  for the transistor based on F-TESADT/PS blend film spin-cast from CB.  $V_D$  was fixed at  $-80 \text{ V}$ .

constant of 2.5, was included for calculating the total capacitance of the dielectric. The average field-effect mobility at the saturation regime was found to be  $7 \times 10^{-3} \text{ cm}^2 \text{ V}^{-1} \text{ s}^{-1}$ . Because the phase-separated interface between F-TESADT and PS, which charges pass through, is as smooth as that of F-TESADT/PMMA blend film spin-cast from DCB, the relatively low field-effect mobility might be due to the low crystallinity of F-TESADT film, as shown in polarized OM image (Figure 8a). This mobility value is more or less similar to that of FET based on a F-TESADT/PMMA blend film fabricated using the same solvent (CB) and is higher than that of FET based on a homo F-TESADT film, which proves that PS can also be used for enhancing field-effect mobility of F-TESADT-based FETs.

Stability poses important issues for the use of transistors in commercial applications.<sup>[24]</sup> The long-term environmental stability of the devices was tested after storage for 5 months under ambient atmosphere (humidity: around 30%, and, temperature: around 25°C), during which time the devices were exposed to laboratory light unintentionally. Figure 13 shows the changes in the transfer characteristics after 5 months. There was a decrease in the on-current (approximately 70%) for the device based on a F-TESADT film. However, the off-current did not vary and the threshold voltage (or turn-on voltage) and subthreshold slope were nearly unchanged. The threshold voltage is known to be related to the impurity or doping level in the semiconductor,

so the absence of any significant threshold voltage shift means that the effects of doping, which can arise when oxygen or an impurity permeate into the semiconductor, are negligible.<sup>[25–27]</sup> The environmental stability of transistors based on F-TESADT/PMMA blends is even more promising. The current on-off ratio, threshold voltage (or turn-on voltage), and subthreshold slope remained nearly the same. The F-TESADT (top)/PMMA (bottom) bilayer structures were fabricated in the bottom-gate device configuration, and the F-TESADT crystals were exposed to ambient conditions. The long-term stability (5 months) of transistors based on the F-TESADT/PMMA blend films is thus quite unexpected. Although the grain size of the crystals, molecular orientation, and interface roughness vary with the solvent, all the devices based on blend films exhibit undeteriorated performances. It can be inferred that the intrinsic molecular parameters of F-TESADT contribute to their long-term stability. The most reactive sites in anthradithiophene are replaced by electron-deficient fluorine atoms, so the thermal and photo-stability of F-TESADT are enhanced over those of unsubstituted TES-ADT.<sup>[5]</sup> In addition, the HOMO level increases from -5.35 to -5.46 eV as a result of the substitution of F atoms (see Figure S7). This deep HOMO level increases the ionization potential, and thus the oxidation and formation of traps (i.e., oxygen doping) are reduced, which results in increased environmental stability.<sup>[2,26]</sup> There is a reduction in the field-effect mobility of the transistor with the F-TESADT film by approximately 50%. However, the decreases

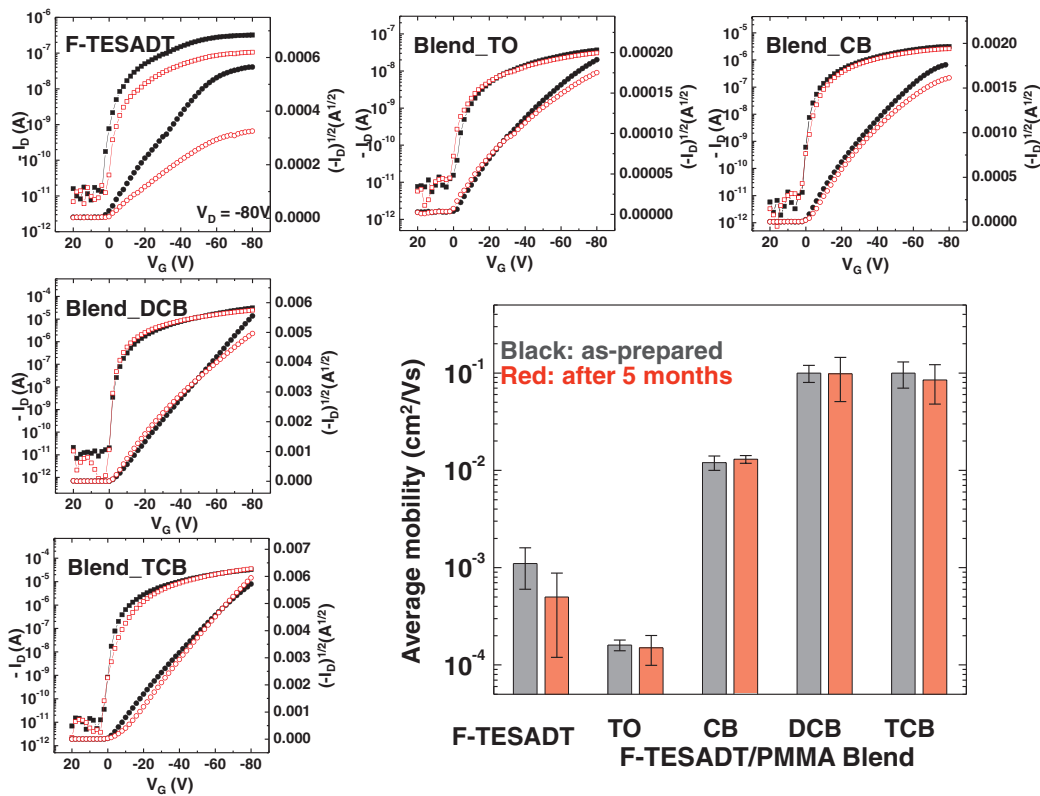


**Figure 13.** Air stability (black: as-prepared, red: after 5 months) of the transistors based on the F-TESADT film (F-TESADT) and the F-TESADT/PMMA blend films spin-cast from various solvents (Blend\_TO: toluene, Blend\_CB: chlorobenzene, Blend\_DCB: 1,2-dichlorobenzene, Blend\_TCB: 1,2,4-trichlorobenzene). The changes in the average field-effect mobilities after 5 months are also summarized.

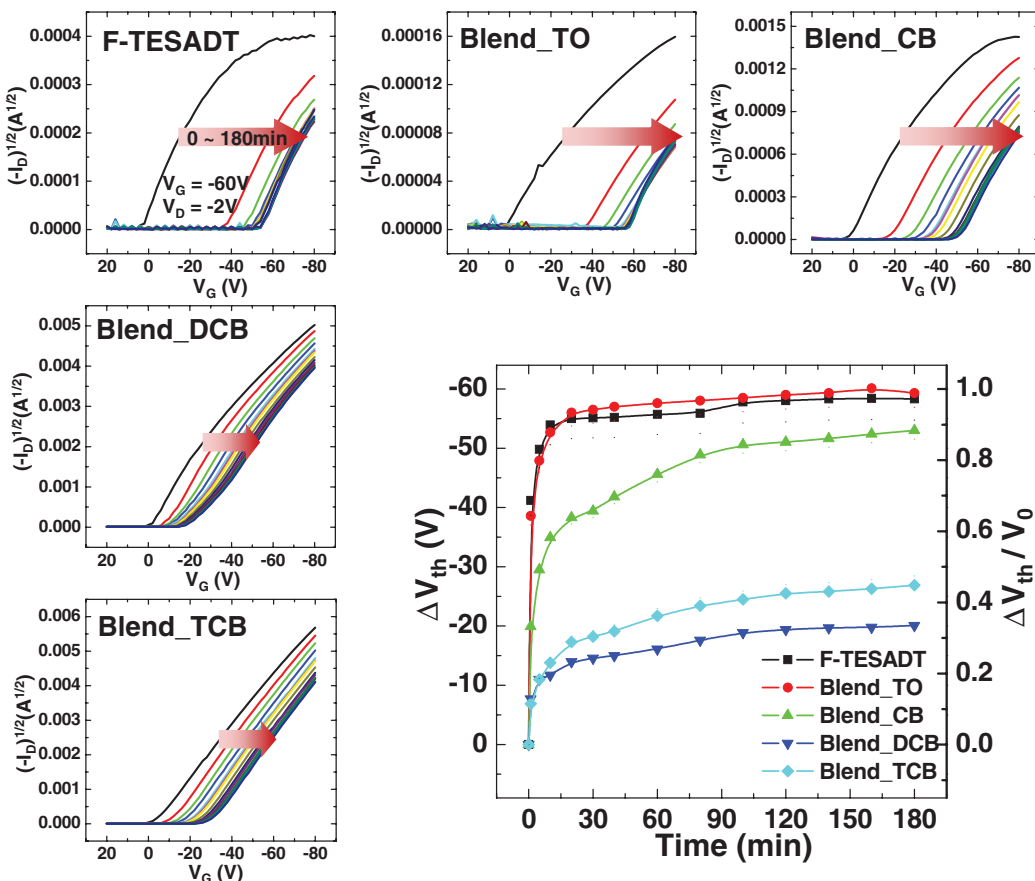


**Figure 14.** Threshold voltage shifts ( $\Delta V_{th}$ ) of the transistors based on the F-TESADT film (F-TESADT) and the F-TESADT/PMMA blend films (Blend\_TO, Blend\_CB, Blend\_DCB, Blend\_TCB) as a function of bias stress time (0–180 min). The bias conditions during stress were fixed at  $V_G = -60$  V,  $V_D = -2$  V and the transfer curves in the saturation regime ( $V_D = -80$  V) were obtained at the following times: 0, 1, 5, 10, 20, 30, 40, 60, 80, 100, 120, 140, 160, and 180 min. The changes in  $\Delta V_{th}$  and  $\Delta V_{th}/V_0$  as a function of stress time are summarized in the bar chart.  $V_0 = V_G - V_{th,0}$ , where  $V_{th,0}$  is the value of  $V_{th}$  at the start of the measurements.

in the field-effect mobilities of the F-TESADT/PMMA blend films are much smaller (Figure 13). We speculate that adsorbed water molecules or ionic mobile impurities in  $\text{SiO}_2$  increase the charge trapping at the interface between F-TESADT and  $\text{SiO}_2$ , which leads to a reduction in environmental stability.<sup>[28–30]</sup> This conjecture is further supported by the observation that most high stability TFT devices are constructed on surface-encapsulated  $\text{SiO}_2$  (i.e.,  $\text{SiO}_2$  treated with octadecyltrichlorosilane).<sup>[27,30–32]</sup> In the F-TESADT/PMMA blend films, the phase-separated PMMA layer on  $\text{SiO}_2$  protects the F-TESADT film from the incursion of ionic mobile impurities. Thus, the TFT devices based on F-TESADT/PMMA blend films undergo little degradation in field-effect performance after exposure of the devices to the atmosphere for 5 months.

Electrical stability under continuous bias conditions is also important for the application of TFTs in commercial display backplanes.<sup>[33]</sup> It is commonly accepted that gate-bias induced charge trapping in immobile states triggers electrical instability.<sup>[29,34]</sup> Such bias stress instability is detrimental to TFT function because gate bias is screened by trapped charges, which results in a reduction in the on-current and shifts in

the threshold voltage ( $\Delta V_{th}$ ) while the field-effect mobility is unchanged.<sup>[35]</sup> Figure 14 shows the changes in the transfer curves after consecutive bias stress ( $V_G = -60$  V,  $V_D = -2$  V, 180 min). To display  $\Delta V_{th}$  more clearly, the changes in the  $(-I_D)^{1/2}$  versus  $V_G$  characteristics after successive measurements are shown in the same graph. The device with a F-TESADT film exhibits a large value of  $\Delta V_{th}$ , which is due to charge trapping at the silanol groups and absorbed water molecules in  $\text{SiO}_2$ .<sup>[30,32,36]</sup> In contrast, the  $\Delta V_{th}$  values of the TFT devices based on F-TESADT/PMMA blend films depend on the solvent. Whereas the  $\Delta V_{th}$  value of the device with a TO blend film is similar to that of the F-TESADT device,  $\Delta V_{th}$  is remarkably lower for the devices with DCB and TCB blend films. The enhanced electrical stabilities of the devices with DCB and TCB blend films might be due to the high crystallinity of their F-TESADT crystals with large grain sizes (Figure 2 and 9) and their smooth interfaces between F-TESADT and PMMA (Figure 6 and 7). Charges are trapped more easily at grain boundaries than inside crystals, so the number of trapping sites is reduced when the grain size is larger.<sup>[37]</sup> The high crystallinity of the F-TESADT crystals and their large grain size in the DCB and TCB blend films contribute

to the improved electrical stability of those devices. For this reason, the devices with DCB and TCB blend films exhibited much higher electrical stability than those with a TO blend film and a F-TESADT film. Note that grain sizes of TO blend film and a F-TESADT film are relatively small and crystal perfections of those films are low.

The roughness of the interface between the semiconductor and the dielectric also affects electrical stability.<sup>[38]</sup> The silanol groups in SiO<sub>2</sub> that can serve as trapping sites are covered by PMMA in the F-TESADT/PMMA blend films. Thus, it is expected that the devices with TO and CB blend films display higher electrical stabilities than that with a F-TESADT film. However, the devices with TO and CB blend films exhibited similar electrical stabilities compared to the device with a F-TESADT film. We surmise that this is caused by the rough interface between F-TESADT and PMMA in the blend films spin-cast from TO and CB (Figure 6 and 7). The rough interface between semiconductor and dielectric serves trap sites for carrier transport, thus leading to the degradation in bias stress stability.<sup>[38]</sup> Thus, the electrical stabilities of the devices based on those films are not as good as that of the device based on the F-TESADT film. Strong emphasis should be placed on the reduction in  $\Delta V_{th}$  by approximately one third that is achieved by blending PMMA with F-TESADT in solution and the phase-separation of PMMA at the film-substrate interface. Although an appropriate solvent is required, our method is a promising approach to the fabrication of transistors with high mobility and excellent environmental and electrical stability. The obtained field-effect mobility (approximately 0.1 cm<sup>2</sup> V<sup>-1</sup> s<sup>-1</sup>), current on-off ratio (approximately 10<sup>7</sup>) and environmental stability (>5 months) are quite suitable for application in display backplanes, such as electrophoretic displays. However, several different factors of electrical stabilities (i.e., off-state stability, cycling test) need to be addressed for the technologically relevance. It is worthy of note that our method for the control of solvent evaporation rate can be utilized to enhance the efficiency of bulkheterojunction organic solar cells, where the electron donor and acceptor are mixed together. However, different types of phase separated structures may be recommended for the exciton dissociation at the donor-acceptor interface and hole/electron transport nearly perpendicular to the substrate surface.

## 4. Conclusions

In summary, we have demonstrated that the use of organic small molecular semiconductor/ insulating polymer blends provides a facile method for the fabrication of high-mobility transistors with environmental and electrical stability. Blending PMMA with F-TESADT reduces the dewetting of F-TESADT and F-TESADT (top)/PMMA (bottom) vertically phase-separated structures are formed by spin-casting the blend solutions in various solvent. By varying the solvent, the solvent evaporation rate can be controlled, and thus the phase-separation characteristics as well as the evolution of the interface microroughness and molecular orientation of the F-TESADT crystals grown on PMMA can be precisely manipulated to optimize charge transport at the phase-separated interface between F-TESADT and

PMMA. As the solvent evaporation rate decreases, the vertical phase separation becomes more obvious and F-TESADT crystals with preferable molecular orientation are formed on the smooth PMMA surface. The performance of the TFT devices based on the blend films are determined by the evaporation-induced phase separation, and these devices were found to exhibit high mobilities with environmental and electrical stability when the solvent evaporation rate was low. The enhancement in the device performances of the blend films over that of the homo F-TESADT film originates from the formation of highly ordered F-TESADT crystals with large grain size on the low-trap PMMA dielectric. Our study shows that the precise control of phase-separation in organic small-molecular semiconductor/insulating polymer blends is important for optimizing the electrical properties of devices based on these films.

## Supporting Information

Supporting Information is available from the Wiley Online Library or from the author.

## Acknowledgements

This work was supported by Global Frontier Research Center for Advanced Soft Electronics and a grant (2011K000176) from the Center for Nanostructured Materials Technology under the 21<sup>st</sup> Century Frontier R&D Programs of the Ministry of Education, Science and Technology, Korea. The authors thank the Pohang Accelerator Laboratory for providing the synchrotron radiation sources at 4B1, 4C2, 8A2, and 10C1 beam lines used in this study.

Received: May 23, 2011

Revised: August 20, 2011

Published online: October 4, 2011

- [1] a) Z. Bao, A. Dodabalapur, A. J. Lovinger, *Appl. Phys. Lett.* **1996**, *69*, 4108; b) M. L. Chabinyc, M. F. Toney, R. J. Kline, I. McCulloch, M. Heeney, *J. Am. Chem. Soc.* **2007**, *129*, 3226; c) H. E. Katz, *Chem. Mater.* **2004**, *16*, 4748; d) H. Sirringhaus, *Adv. Mater.* **2005**, *17*, 2411; e) I. Osaka, G. Sauve, R. Zhang, T. Kowalewski, R. D. McCullough, *Adv. Mater.* **2007**, *19*, 4160; f) H. Usta, C. Risko, Z. M. Wang, H. Huang, M. K. Deliomeroglu, A. Zhukhovitskiy, A. Facchetti, T. J. Marks, *J. Am. Chem. Soc.* **2009**, *131*, 5586; g) H. Yan, Z. H. Chen, Y. Zheng, C. Newman, J. R. Quinn, F. Dotz, M. Kastler, A. Facchetti, *Nature* **2009**, *457*, 679; h) Y. Y. Noh, N. Zhao, M. Caironi, H. Sirringhaus, *Nat. Nanotechnol.* **2008**, *3*, 58; i) P. Gao, D. Beckmann, H. N. Tsao, X. L. Feng, V. Enkelmann, M. Baumgarten, W. Pisula, K. Mullen, *Adv. Mater.* **2009**, *21*, 213; j) D. H. Kim, Y. D. Park, Y. S. Jang, H. C. Yang, Y. H. Kim, J. I. Han, D. G. Moon, S. J. Park, T. Y. Chang, C. W. Chang, M. K. Joo, C. Y. Ryu, K. W. Cho, *Adv. Funct. Mater.* **2005**, *15*, 77; k) Y. D. Park, D. H. Kim, Y. Jang, J. H. Cho, M. Hwang, H. S. Lee, J. A. Lim, K. Cho, *Org. Electron.* **2006**, *7*, 514.
- [2] a) I. McCulloch, M. Heeney, C. Bailey, K. Genevicius, I. Macdonald, M. Shkunov, D. Sparrowe, S. Tierney, R. Wagner, W. M. Zhang, M. L. Chabinyc, R. J. Kline, M. D. McGehee, M. F. Toney, *Nat. Mater.* **2006**, *5*, 328; b) B. S. Ong, Y. L. Wu, P. Liu, S. Gardner, *J. Am. Chem. Soc.* **2004**, *126*, 3378.
- [3] a) J. E. Anthony, J. S. Brooks, D. L. Eaton, S. R. Parkin, *J. Am. Chem. Soc.* **2001**, *123*, 9482; b) A. L. Briseno, Q. Miao, M. M. Ling,

- C. Reese, H. Meng, Z. N. Bao, F. Wudl, *J. Am. Chem. Soc.* **2006**, *128*, 15576; c) Q. Miao, X. L. Chi, S. X. Xiao, R. Zeis, M. Lefenfeld, T. Siegrist, M. L. Steigerwald, C. Nuckolls, *J. Am. Chem. Soc.* **2006**, *128*, 1340; d) K. C. Dickey, J. E. Anthony, Y. L. Loo, *Adv. Mater.* **2006**, *18*, 1721; e) D. H. Kim, D. Y. Lee, H. S. Lee, W. H. Lee, Y. H. Kim, J. I. Han, K. Cho, *Adv. Mater.* **2007**, *19*, 678; f) W. H. Lee, D. H. Kim, Y. Jang, J. H. Cho, M. Hwang, Y. D. Park, Y. H. Kim, J. I. Han, K. Cho, *Appl. Phys. Lett.* **2007**, *90*, 132106.
- [4] M. M. Payne, S. R. Parkin, J. E. Anthony, C. C. Kuo, T. N. Jackson, *J. Am. Chem. Soc.* **2005**, *127*, 4986.
- [5] S. Subramanian, S. K. Park, S. R. Parkin, V. Podzorov, T. N. Jackson, J. E. Anthony, *J. Am. Chem. Soc.* **2008**, *130*, 2706.
- [6] a) S. Allard, M. Forster, B. Souharce, H. Thiem, U. Scherf, *Angew. Chem., Int. Ed.* **2008**, *47*, 4070; b) M. Mas-Torrent, C. Rovira, *Chem. Soc. Rev.* **2008**, *37*, 827; c) J. E. Anthony, J. Gierschner, C. A. Landis, S. R. Parkin, J. B. Sherman, R. C. Bakus, *Chem. Commun.* **2007**, *4746*; d) J. E. Anthony, *Chem. Rev.* **2006**, *106*, 5028.
- [7] J. A. Lim, H. S. Lee, W. H. Lee, K. Cho, *Adv. Funct. Mater.* **2009**, *19*, 1515.
- [8] a) M. B. Madec, D. Crouch, G. R. Llorente, T. J. Whittle, M. Geoghegan, S. G. Yeates, *J. Mater. Chem.* **2008**, *18*, 3230; b) T. Ohe, M. Kuribayashi, R. Yasuda, A. Tsuboi, K. Nomoto, K. Satori, M. Itabashi, J. Kasahara, *Appl. Phys. Lett.* **2008**, *93*, 053303; c) J. Kang, N. Shin, D. Y. Jang, V. M. Prabhu, D. Y. Yoon, *J. Am. Chem. Soc.* **2008**, *130*, 12273; d) J. Smith, R. Hamilton, M. Heeney, D. M. de Leeuw, E. Cantatore, J. E. Anthony, I. McCulloch, D. D. C. Bradley, T. D. Anthopoulos, *Appl. Phys. Lett.* **2008**, *93*, 253301.
- [9] R. Hamilton, J. Smith, S. Ogier, M. Heeney, J. E. Anthony, I. McCulloch, J. Veres, D. D. C. Bradley, T. D. Anthopoulos, *Adv. Mater.* **2009**, *21*, 1166.
- [10] a) L. L. Chua, P. K. H. Ho, H. Sirringhaus, R. H. Friend, *Adv. Mater.* **2004**, *16*, 1609; b) A. C. Arias, *Polym. Rev.* **2006**, *46*, 103; c) A. C. Arias, F. Endicott, R. A. Street, *Adv. Mater.* **2006**, *18*, 2900; d) A. Salleo, A. C. Arias, *Adv. Mater.* **2007**, *19*, 3540; e) L. Qiu, J. A. Lim, X. Wang, W. H. Lee, M. Hwang, K. Cho, *Adv. Mater.* **2008**, *20*, 1141.
- [11] S. Goffri, C. Muller, N. Stigelin-Stutzmann, D. W. Breiby, C. P. Radano, J. W. Andreasen, R. Thompson, R. A. J. Janssen, M. M. Nielsen, P. Smith, H. Sirringhaus, *Nat. Mater.* **2006**, *5*, 950.
- [12] W. H. Lee, J. A. Lim, D. Kwak, J. H. Cho, H. S. Lee, H. H. Choi, K. Cho, *Adv. Mater.* **2009**, *21*, 4243.
- [13] D. J. Gundlach, J. E. Royer, S. K. Park, S. Subramanian, O. D. Jurchescu, B. H. Hamadani, A. J. Moad, R. J. Kline, L. C. Teague, O. Kirillov, C. A. Richter, J. G. Kushmerick, L. J. Richter, S. R. Parkin, T. N. Jackson, J. E. Anthony, *Nat. Mater.* **2008**, *7*, 216.
- [14] J. Smith, R. Hamilton, Y. B. Qi, A. Kahn, D. D. C. Bradley, M. Heeney, I. McCulloch, T. D. Anthopoulos, *Adv. Funct. Mater.* **2010**, *20*, 2330.
- [15] *Chemical Properties Handbook*, (Ed: C. L. Yaws), McGraw-Hill, New York **1999**.
- [16] A. Salleo, R. A. Street, *J. Appl. Phys.* **2003**, *94*, 4231.
- [17] P. H. Wobkenber, J. Ball, F. B. Kooistra, J. C. Hummelen, D. M. de Leeuw, D. D. C. Bradley, T. D. Anthopoulos, *Appl. Phys. Lett.* **2008**, *93*, 013303.
- [18] K. Tanaka, A. Takahara, T. Kajiyama, *Macromolecules* **1996**, *29*, 3232.
- [19] G. R. Strobl, *The Physics of Polymers: Concepts for Understanding their Structures and Behavior*, Springer, Berlin, New York **1996**.
- [20] R. A. L. Jones, R. W. Richards, *Polymers at Surfaces and Interfaces*, Cambridge University Press, Cambridge, New York **1999**.
- [21] a) Y. D. Park, J. A. Lim, H. S. Lee, K. Cho, *Mater. Today* **2007**, *10*, 46; b) D. Braga, G. Horowitz, *Adv. Mater.* **2009**, *21*, 1473.
- [22] A. E. Lita, J. E. Sanchez, *Phys. Rev. B* **2000**, *61*, 7692.
- [23] a) D. M. DeLongchamp, B. M. Vogel, Y. Jung, M. C. Gurau, C. A. Richter, O. A. Kirillov, J. Obrzut, D. A. Fischer, S. Sambasivan, L. J. Richter, E. K. Lin, *Chem. Mater.* **2005**, *17*, 5610; b) H. Yang, S. W. LeFevre, C. Y. Ryu, Z. N. Bao, *Appl. Phys. Lett.* **2007**, *90*, 172116.
- [24] Y. L. Loo, I. McCulloch, *MRS Bull.* **2008**, *33*, 653.
- [25] a) D. M. de Leeuw, M. M. J. Simenon, A. R. Brown, R. E. F. Einerhand, *Synth. Met.* **1997**, *87*, 53; b) S. Ogawa, T. Naijo, Y. Kimura, H. Ishii, M. Niwano, *Appl. Phys. Lett.* **2005**, *86*, 252104.
- [26] B. S. Ong, Y. L. Wu, Y. N. Li, P. Liu, H. L. Pan, *Chem. Eur. J.* **2008**, *14*, 4766.
- [27] D. Kumaki, M. Yahiro, Y. Inoue, S. Tokito, *Appl. Phys. Lett.* **2007**, *90*, 133511.
- [28] D. B. A. Rep, A. F. Morpurgo, W. G. Sloof, T. M. Klapwijk, *J. Appl. Phys.* **2003**, *93*, 2082.
- [29] S. J. Zilker, C. Detcheverry, E. Cantatore, D. M. de Leeuw, *Appl. Phys. Lett.* **2001**, *79*, 1124.
- [30] C. Goldmann, D. J. Gundlach, B. Batlogg, *Appl. Phys. Lett.* **2006**, *88*, 063501.
- [31] a) T. Umeda, S. Tokito, D. Kumaki, *J. Appl. Phys.* **2007**, *101*, 054517; b) J. Locklin, M. M. Ling, A. Sung, M. E. Roberts, Z. N. Bao, *Adv. Mater.* **2006**, *18*, 2989; c) T. Miyadera, S. D. Wang, T. Minari, K. Tsukagoshi, Y. Aoyagi, *Appl. Phys. Lett.* **2008**, *93*, 033304.
- [32] T. N. Ng, J. A. Marohn, M. L. Chabinyc, *J. Appl. Phys.* **2006**, *100*, 084505.
- [33] R. A. Street, *Technology and Applications of Amorphous Silicon*, Springer, New York **2000**.
- [34] a) M. Matters, D. M. de Leeuw, P. T. Herwig, A. R. Brown, *Synth. Met.* **1999**, *102*, 998; b) R. A. Street, A. Salleo, M. L. Chabinyc, *Phys. Rev. B* **2003**, *68*, 085316.
- [35] S. G. J. Mathijssen, M. Colle, H. Gomes, E. C. P. Smits, B. de Boer, I. McCulloch, P. A. Bobbert, D. M. de Leeuw, *Adv. Mater.* **2007**, *19*, 2785.
- [36] a) G. Gu, M. G. Kane, J. E. Doty, A. H. Firester, *Appl. Phys. Lett.* **2005**, *87*, 243512; b) C. Goldmann, C. Krellner, K. P. Pernstich, S. Haas, D. J. Gundlach, B. Batlogg, *J. Appl. Phys.* **2006**, *99*, 034507.
- [37] a) D. W. Li, E. J. Borkent, R. Nortrup, H. Moon, H. Katz, Z. N. Bao, *Appl. Phys. Lett.* **2005**, *86*, 042105; b) W. L. Kalb, T. Mathis, S. Haas, A. F. Stassen, B. Batlogg, *Appl. Phys. Lett.* **2007**, *90*, 092104; c) M. Tello, M. Chiesa, C. M. Duffy, H. Sirringhaus, *Adv. Funct. Mater.* **2008**, *18*, 3907.
- [38] K. Suemori, S. Uemura, M. Yoshida, S. Hoshino, N. Takada, T. Kodzasa, T. Kamata, *Appl. Phys. Lett.* **2008**, *93*, 033308.